Computational Investigation of Spacecraft Recovery via Rotary Wings: A Study on Autorotation

João Pedro Sousa Gaspar

joao.p.gaspar@tecnico.ulisboa.pt

Instituto Superior Técnico, Lisboa, Portugal

June 2025

Abstract

Using rotary wings for spacecraft recovery could be an efficient solution for the recovery of spacecraft. In the past, several studies were conducted to examine the feasibility of such a system, and despite some limitations, the capability of recovering spacecraft with rotary wings has been demonstrated. The lack of experimental tests and the need for more in-depth analysis models led to the current development of a Matlab-based simulator. The aim was to study the dynamics of a spacecraft with rotary wings. Detailed methods for analyzing the rotor in autorotation, both in axial flight and gliding flight, were described. This involved using the Blade Element Theory (BET) adapted with an aerodynamic airfoil model that combined an extrapolated neural network for large angles of attack. Studies showed how root cut-out, taper, and blade twist affect the flight dynamics and identified the inherent limitations due to their geometry. Furthermore, studies were conducted on the use of multiple airfoils. Finally, autorotational flight was perturbed using a simple wind gust model. This work demonstrates several milestone advances in the study and understanding of the system. Although many challenges still need to be overcome, the computational work developed proves to be a fundamental step for future research.

Keywords: Autorotation, Recovery, Wind Gust, Aerodynamics, Flight Dynamics

1. Introduction

Over decades the space race has conducted major changes in scientific exploration, from the space race between United States and Russia to the construction of the International Space Station (ISS). The space race has been a driving force for technological advancements. Nowadays, the global economy is facing a players change from governmental organizations to private companies leading to a profitable market with a growing interest in space exploration [1].

The technological advancements are futher refined, once the private interest in aerospace industry is to make it profitable [2]. Turning a space mission into a profitable business, the reusability of spacecraft is a key factor. To illustrate the importance of reusability, NASA Apollo program was a technological advancement in which the spacecraft was used multiple times for different space missions. However, the reusibilty of spacecraft is somethig that has be considered over the years, and many differenent technologies were used such as a parachute system to recover astronaut capsules [3] and higly complex trust vector controll system.

Using a rotary wing as an aerodynamic decelar-tor is not a new concept [4]. Over the years, many different rotary wing configurations have been proposed and tested [5, 6]. Nowadays, there are several other ongoing projects. The ARMADA concept [7] started to be developed in 2008 by an international colaboration led by the European Space Agency (ESA) studying the feasibility of using a rotor for space recovery. The interest and development of this recovery system has led to the creation of academic projects such as the DAEDALUS project [8].

It is clear that there is an current interest in the use of rotary wings, particularly when operating under the phenomenon of autorotation. So, the main goal is to improve the knowledge of previous works by conducting several studies, including a parametric study and the wind gust effect.

2. Vehicle and Rotor dynamics

The vehicle model is based in a point-mass model for the payload with a rotor coupled. With this model the goal is to understand how the rotor performes when it comes to recover a mass under the influence of the gravitational force.

For the development of the mathematical model, five reference frames (see Fig. 1) are used in this study: O^i, the inertial (navigation) frame fixed to a

point on Earth; O^r, the body frame at the vehicle's center of gravity; O^b, aligned with the blade span; O^e, the blade element frame along the radius; and O^a, the aerodynamic frame used for local forces and moments.
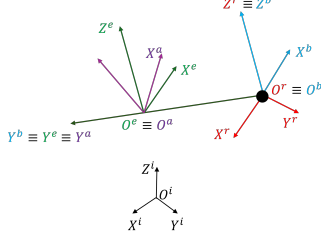

Figure 1: Illusttration of the reference frame

For the equations of motion, Newton's second law is used. It states, for translational motion, that the sum of external forces is equal to the change in linear momentum

$$\mathbf{F}^i = \frac{\mathrm{d}}{\mathrm{d}t}(M\mathbf{V})^i \qquad (1)$$

where M represent the system mass and, for rotational motion, that the sum of external moments $\mathbf{M}^r$ regarding its center of mass is equal to the rate of change in angular momentum,

$$\mathbf{M}^r = \frac{\mathrm{d}}{\mathrm{d}t}([\mathbf{I}]\,\boldsymbol{\omega})^r + \boldsymbol{\omega} \times ([\mathbf{I}]\,\boldsymbol{\omega})^r \qquad (2)$$

where $[\mathbf{I}]$ is the inertia tensor. Furthermore, the rotor's rotation is decoupled from the vechicle's motion, and the rotor's dynamics is described by Eq. 3

$$\frac{\mathrm{d}\Omega}{\mathrm{d}t} = \frac{T}{I_{zz}} \qquad (3)$$

where T is the rotor's torque, I_{zz} is the rotor's moment of inertia around the z-axis.

3. Blade Element Theory (BET)

In order to compute the blade force and torque, the BET is a quasi-2D airfoils blade section based method, a simple solution for initial rotor designs [9].
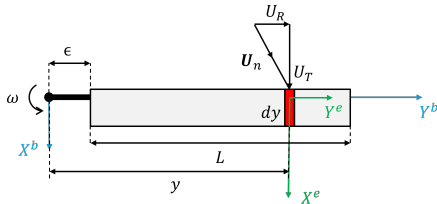

Figure 2: BET model

In Fig. 2, the general geometry of a blade which is divided into elements is presented, highlighting a typical element in red. The blade reference frame and the local coordinate systems are also shown. Fig. 3 displays in detail an individual element, with the local velocity vector and the aerodynamic forces represented.
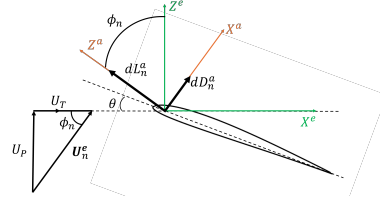

Figure 3: Blade element with flow enviroment and forces aplied.

The velocity vector in the element's reference frame, O^e, Eq. 4

$$\mathbf{U}_n^e = \begin{bmatrix} U_t & U_r & U_p \end{bmatrix}^T \qquad (4)$$

where U_t, U_r and U_p are the tangential, radial and vertical components respectively. By the principle of independence, the radial velocity, U_r, is not considered [9], and the magnitued of the airfoil velocity is computed as Eq. 5

$$U_n = \sqrt{U_t^2 + U_p^2} \equiv \|\mathbf{U}_n^e\|. \qquad (5)$$

The drag force is given by Eq. 6,

$$\mathrm{d}D_n^a = \frac{1}{2}\rho c U_n^2 C_d, \qquad (6)$$

where C_d is the drag coefficient, ρ is the air density, and c the airfoil cord. The vertical compenent (in Z^a axis) or lift force is computed as Eq. 7,

$$\mathrm{d}L_n^a = \frac{1}{2}\rho c U_n^2 C_l. \qquad (7)$$

So the force vector int the aerodynamic reference frame, O^a, is

$$\mathrm{d}\mathbf{F}_n^a = \begin{bmatrix} \mathrm{d}D_n^a & 0 & \mathrm{d}L_n^a \end{bmatrix}^T \qquad (8)$$

The force vector can be written in the rotor frame, O^r, using a rotation matrix from the aerodynamic reference frame, O^a, $\boldsymbol{R}_{a\to r}^{\mathrm{ot}}$. So, for the blade m, the force vector is given by the integration over the blade span, S_b as Eq. 9,

$$\mathbf{F}_m^r = \int_\epsilon^{S_b+\epsilon} \mathrm{d}\mathbf{F}_n^r \mathrm{d}y = \int_\epsilon^{S_b+\epsilon} \boldsymbol{R}_{a\to r}^{\mathrm{ot}}\, \mathrm{d}\mathbf{F}^a \mathrm{d}y, \qquad (9)$$

and for the rotor torque, Eq. 10,

$$\mathbf{Q}_m^r = \int_\epsilon^{S_b+\epsilon} \mathrm{d}\mathbf{Q}_n^r \mathrm{d}y = \int_\epsilon^{S_b+\epsilon} \mathbf{r} \times \left(\boldsymbol{R}_{a\to r}^{\mathrm{ot}}\, \mathrm{d}\mathbf{F}^a \right) \mathrm{d}y. \qquad (10)$$

The total force and torque for the rotor is the sum of the forces and torques of each blade, and the previous equations can be extended for the total blade number, N_b, and azimutal distributions as a average of the blades in a revolution, Eq. 11

$$\mathbf{F}_{rotor}^r = \frac{N_b}{N_\psi} \sum_{m=1}^{N_\psi} \int_\epsilon^{S_b+\epsilon} \boldsymbol{R}_{a \to r}^{ot} \, d\mathbf{F}^a dy. \quad (11)$$

The same is done for the rotor torque, Eq. 12,

$$\mathbf{Q}_{rotor}^r = \frac{N_b}{N_\psi} \sum_{m=1}^{N_\psi} \int_\epsilon^{S_b+\epsilon} \mathbf{r} \times \left(\boldsymbol{R}_{a \to r}^{ot} \, d\mathbf{F}^a \right) dy. \quad (12)$$

4. Aerodynamic Model

The contribution of 2D airfoil sections to the BETs introduced through an aerodynamic model combining a Neural Network (NN) and the AERODAS model for computing lift and drag, respectively,

$$C_l \equiv C_l(\alpha, Re) \quad \text{and} \quad C_d \equiv C_d(\alpha, Re), \quad (13)$$

as functions of the angle of attack, α, and the Reynolds number, Re, since this work does not consider compressible effects. Under autorotation, the rotor undergoes a wide range of angles of attack, and the Reynolds number varies; therefore, a model is needed that can predict the aerodynamic forces across a wide range of conditions.

The NeuralFOIL [10] is an NN model trained with XFOIL data for a wide range of Re. Therefore, the NN exhibits a low confidence level for post-stall angles, as XFOIL is not able to compute in this range of angles of attack. So, to overcome this issue, the AERODAS model [11] is introduced. The AERODAS model is a model that can predict aerodynamic forces through a simple mathematical expression, making the aerodynamic model extremely fast. Additionally, it includes extrapolation to the post-stall regime, which provides greater reliability to the aerodynamic model.

5. Computational Methods

Regarding the computational methods, the Runge-Kutta 4th order method (RK4) was implemented to overcome the accuracy and stability problems of the Euler method, solving the non-linear ordinary differential equations (ODEs) in Eqs. 1 and 2. For instance, the BET model is implemented using the trapezoidal rule to achieve better accuracy and balance computational effort.

6. Validation and verification

The reuslts from Brindejonc et al. (2007) [12] conducted wind tunnel of setup of a 2-bladed with no
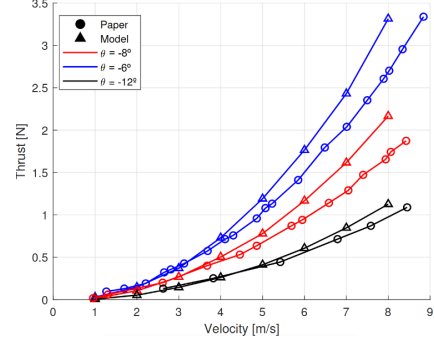

Figure 4: Thrust force comparison with [12]

pitch-flap coupling and no precone, are used to validate the rotor model.

Fig. 4 presents the comparison, and results show a good agreement between the experimental data and the numerical results. The error between the two sets of data reveals a variation in the thrust force, with a maximum error found of 27.4%.

Overall, the 2D aerodynamic model considered in this work overestimates the lift and drag coefficients. Nonetheless, the computational time versus accuracy trade-off is quite acceptable for this work, as the results are in good agreement with the experimental data.

The primary objective of this work is to enhance the model and knowledge gained from previous research conducted by Marques [13]. The key differences are the numerical methods used for both the ODE integration and the BET model integration, as well as the 2D aerodynamic model.
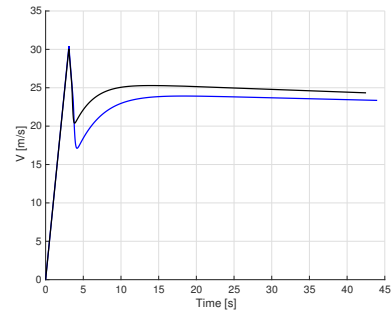

Figure 5: Vehicle velocity comparison with [13]

Although the terminal velocities are slightly different, as observed in Figs. 5 and 6 show that the vehicle dynamics exhibit the same profile, where a reduction in velocity at the rotor's opening is followed by an increase until the vehicle reaches its terminal velocity.

The aerodynamic model used in this work presents an opening rotor force and, consequently, torque with a higher magnitude than the one presented in [13]. This explains the reduction in ve-
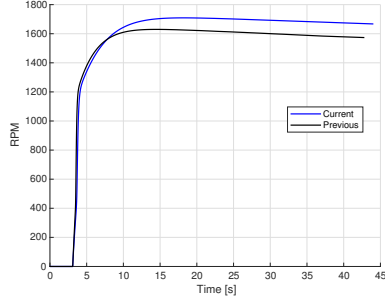
3

Figure 6: Rotor velocity comparison with [13]

locity observed. Also, Fig. 6 shows that the rotor is performing at a higher rotational speed. The autorotation phenomenon is achieved in distinct time instants once the torque is zero, later in the simulation for the present work model.

When a vehicle comes from space or higher altitudes, the atmospheric influence plays a vital role in the rotor performance. Here,it introduces a comparison with the Daedalus project [8], where a vehicle is recovered from an altitude of 75 km.

The results are in agreement with the experimental and simulation data from [8] up to an altitude of 20 km. Beyond this point, slight differences appear, which are clearly observed in the velocity profile, Fig. 7.
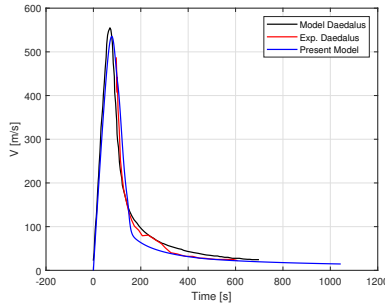
Figure 7: Vehicle velocity comparison with experimental and simulation data from [8]

The Daedalus project also utilises AERODAS, but the input data may originate from various sources, which cannot be confirmed since the master's thesis that initiated the Daedalus project was not published. Nonetheless, it proves a useful model for high altitudes, enabling further investigation using the ISA model.

The autorotation in glide flight data was not found in the literature for further comparison . Nevertheless, the BET model in a gliding flight can be verified in contrast to the theory presented in many textbooks. From Fig. 8, two key considerations shall be done: 1) On the advancing side of the rotor, near the tip, the tangential velocity, U_t, is at

its maximum due to the addition of the rotational and translational components. 2) On the retreating side, near the root, the tangential velocity is significantly lower, as the translational component subtracts from the rotational velocity.
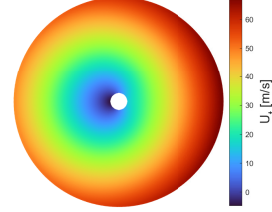

Figure 8: Tangecial velocity in element reference frame, O^e

As expected, the inflow angle, ϕ, is negative due to the descending motion. In the reverse flow region, the inflow angle shows values of up to $-180°$. In contrast, the rotor's distribution angles of attack, α, are always positive. In the reverse flow region, the angles of attack are higher $180°$ since the inflow angle is added to the pitch angle, θ.
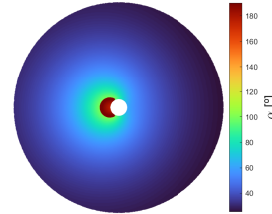

Figure 9: Baseline simulation outputs for autorotation analysis and comparison

From Fig. 9, the tip velocity effect is observable, where near the tip, the tangential velocity is predominant due to higher speeds, and the resultant angle of attack is lower than a region with lower tangential velocity.

Finally, Fig. 10 shows the loads distributions in the rotor reference frame, O^r, computed as in Eq. 11. As a reverse flow region emerges, it leads to negative aerodynamic forces and thrust losses. High vertical force values are concentrated at the blade tip, and a significant force difference is observed on the advancing side of the blade. The total force in the x-axis is a non-uniform distribution, where the retreating side generates less force than the advancing side. On the other hand, the y-axis force is zero.

7. Mesh study

Carrying out the mesh study, the discretisation time step, Δt, showed that for all cases from 0.001 to 90
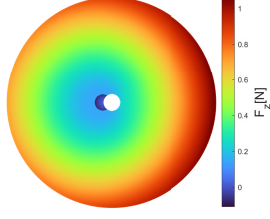
4

Figure 10: Rotor forces distribution

ms, all results achieve the same autorotation state. For higher Δt values, the RK4 method showed instabilities. From Fig. 11, it is possible to conclude that for the rotor opening, the higher relative errors appear for lower time discretisation.
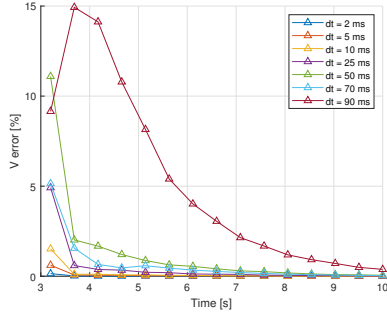

Figure 11: Relative error over the simulation time for different time steps for the vehicle velocity during the rotor opening

For instance, the rotor mesh discretisation showed that a relatively low error is achieved with few azimuthal points and blade elements. This conclusion shows an interesting improvement in the rotor analysis with the trapezoidal rule.

8. Parametric Study

For the parametric study, a baseline simulation was defined and is represented in the following studies as a dashed line.

The root cut-out was analyzed in two cases. In **Case #1**, the blade span S_b is kept constant while a root distance ϵ is added, effectively increasing the rotor radius. In this case, the cut-out is defined as a percentage of the blade span added beyond the original radius, but both the blade span and mass remain unchanged. In **Case #2**, the rotor radius is fixed, and the root is cut by a percentage of the radius. This reduces the blade span and mass, thereby lowering the weight.

In **Case #1**, where the blade span, S_b, is fixed and the cut-out ϵ increases the rotor radius, the rotor's moment of inertia increases due to the larger distance between the blade's centre of mass and the rotation axis. Consequently, the rotor rota-
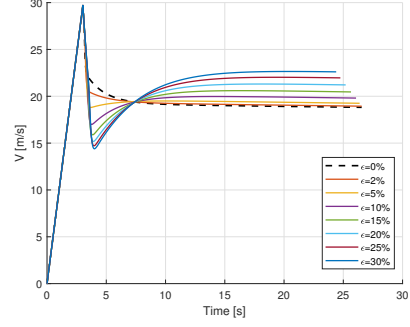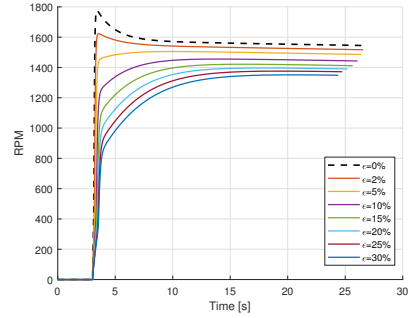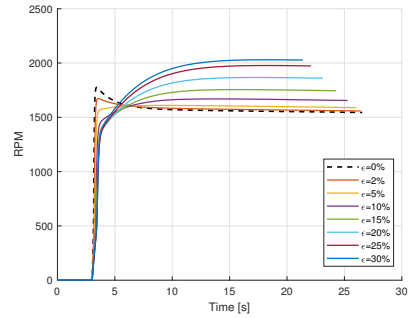

(a) Case #1
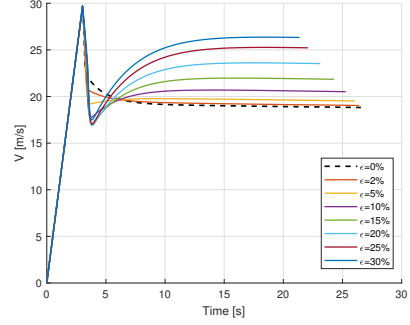
(b) Case #2

Figure 12: Velocity profile for the variation of the blade root cut-out, for cases #1 and #2

(a) Case #1

(b) Case #2

Figure 13: Rotor velocity profile for the variation of the blade root cut-out, for cases #1 and #2

tional speed is lower for the autorotation regime, as shown in Fig. 13(a). The vehicle's terminal velocity increases with ϵ (Fig. 13(a)), indicating less effectiveness in reducing the descent velocity. The

5

initial thrust force is similar across all cases, but its development differs (Fig. 14(a)), reflecting the influence of increased inertia on rotor acceleration. The torque is higher at the start, but due to the larger inertia, the rotor spins slower, and the autorotation operation state is achieved later.

In **Case #2**, with a fixed rotor radius and a reduction in blade span and mass, the decrease in mass causes a significant reduction in rotational inertia. This result has a substantial increase in rotor rotational, as shown in Fig. 13(b). The initial thrust force decreases proportionally with the span reduction, Fig. 14(b), while the torque remains almost constant for different ϵ values (Fig. 15(b)). The vehicle terminal velocity also increases with the cut-out percentage, indicating the reduced capability of the rotor to slow down the descent, Fig. 12(b).
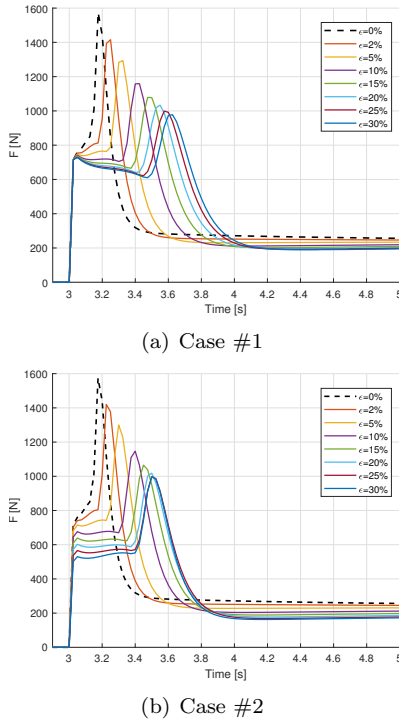

(a) Case #1

(b) Case #2

Figure 14: Rotor thrust profile for the variation of the blade root cut-out, for cases #1 and #2, zoomed in the rotor opening time interval

The blade taper, defined as the variation of the airfoil chord along the blade length, critically influences the blade's aerodynamics. Prior to analyzing the taper constant, λ_C, is introduced as

$$\lambda_C = \frac{c_{tip}}{c_{root}}, \tag{14}$$

where c_{tip} and c_{root} are the chord lengths at the blade tip and root, respectively. The chord variation along the blade span y is given by the linear function.

$$c(y) = c_{\text{root}}\left(1 - (1 - \lambda_C)\frac{y}{L}\right). \tag{15}$$
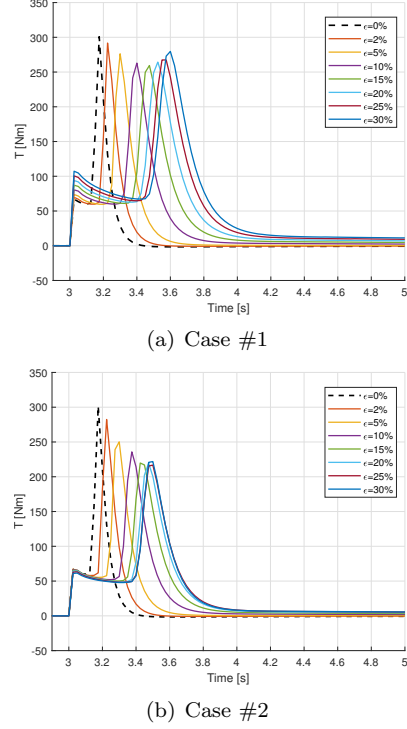

(a) Case #1

(b) Case #2

Figure 15: Rotor torque profile for the variation of the blade root cut-out, for cases #1 and #2, zoomed in the rotor opening time interval

Results show that the reduction in blade surface does not prevent the rotor from reaching autorotation. For all λ_C values tested, the vehicle descends at a constant velocity with a steady vertical velocity and rotor speed (Figs. 16(a) and 16(b)).

The chord directly affects the elementary aerodynamic forces dD and dL (Eqs. 6 and 7), so reducing chord length decreases lift and drag due to smaller blade surface area. At rotor deployment ($t = 3\,\text{s}$), rotor thrust increases with λ_C, being highest for $\lambda_C = 1$ and lowest for $\lambda_C = 0.05$ (Fig. 17(a)).

Lower blade forces correspond to lower torque (Fig. 17(b)), causing a longer time for the blades to reach unstalled operation. Torque peaks appear later for smaller λ_C, which delays the rotor from reaching unstalled operation.

Blade twist varies the pitch along the blade and affects rotor performance [14]. A linear twist distribution is used as an approximation [9]. Positive twist rate, dθ/dy, with a lower pitch near the root and higher at the tip, helps avoid negative angles of attack that cause downward forces, supporting autorotation [15], and then only positive twist rates were considered.

The simulations of the axial descent with the twist rates considered results in a reduction of descent velocity (see Fig. 18(a)), but for the dθ/dy = 10, 12, 15 °/m, Fig. 18(b), shows a considerable difference in rotor speed. For dθ/dy = 2, 5, 7 °/m,
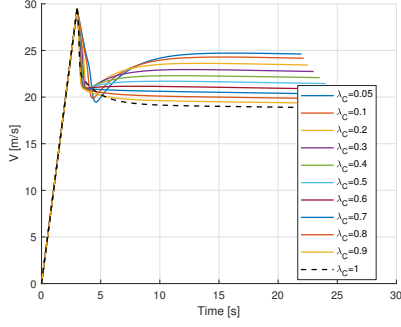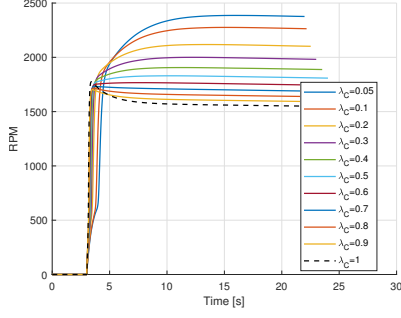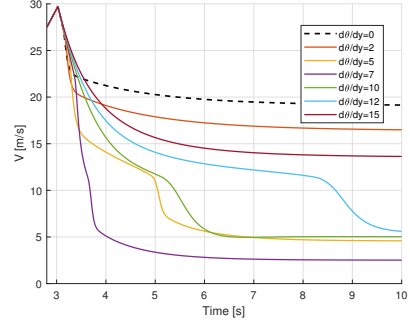
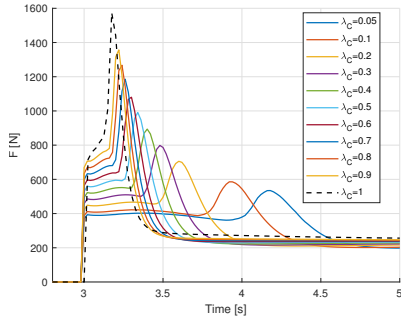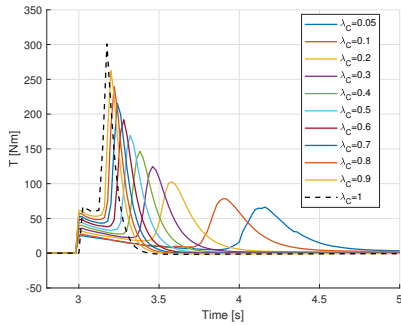Figure 16: Vehicle velocity, in m (a) and rotor velocity in RPM (B)

Figure 17: Rotor's force in N (a); and torque in Nm (B)

Figure 18: Vehicle velocity in m/s (a); Rotor speed in RPM (b), for different twist rates

show a similar rotor speed as the baseline with 0 °/m twist rate. In aprticulary, $d\theta/dy = 5, 7$ °/m where a significant velocity reduction is observed.

A significant velocity reduction makes the rotor operate in the Vortex Ring State (VRS). From Fig. 19(a), the force evolution over time is verified as a double force peak where the first means the transition from stalled to unstalled operations and the second force peak is the transition from the Windmill Break State (WBS) to VRS. Moreover, Fig. 19(b) shows negative torque values coincident with when the rotor enters the VRS and delaying the rotor from reaching the autorotation operation.

Going back to the results for $d\theta/dy = 10, 12, 15$ °/m, a significant difference in rotor velocity is seen in Fig. 18(b). The low rotor velocity profiles show that the rotor reaches the autorotation (see Fig. 18(b)), but it is not clear if the rotor is working in a stable autorotation descent. The low rotor velocities came from low torques, which did not accelerate the rotor enough to transition from stall blades to unstalled blades. In an instant where rotation speeds are constant, the angle of attack did not reach the pre-stall regime, never achieving a stable autorotation descent.

As previously said, the increase in rotor velocity leads to a higher inflow angle, resulting in higher tangential velocity. With $d\theta/dy = 10, 12, 15$ °/m, the rotor only operates in post-stall angles. On the other hand, $d\theta/dy = 2, 5, 7$ °/m the negative angles at the tip of the blade increase, reaching positive values near the tip, which translate in a lift instead of downforce.
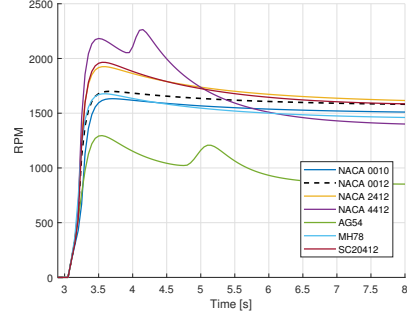
In addition, a last point should be added

7
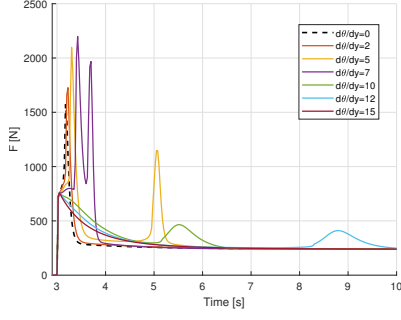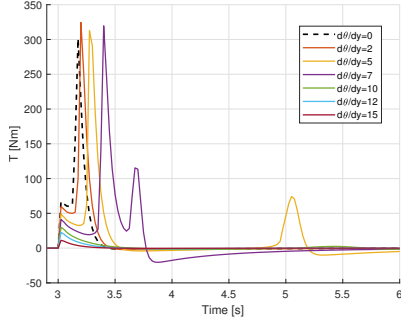
Figure 19: Rotor's force in N (a); and torque in Nm (B), for different twist rates

Figure 20: Vehicle velocity in m/s (a); Rotor speed in RPM (b), for different twist rates

to the results of the simulations for $d\theta/dy = 10, 12, 15$ °/m. In Fig. 19(a), the cases with $d\theta/dy = 10$ and 12 °/m (green and light blue lines, respectively) show a peak force that should be commented. It occurs for the same reason why there is a double peak in other twist rate values: the transition from WBS to VRS. Compared with Fig. 18(a), the pick coincides with the time interval where the vehicle axial velocity reaches the VRS.
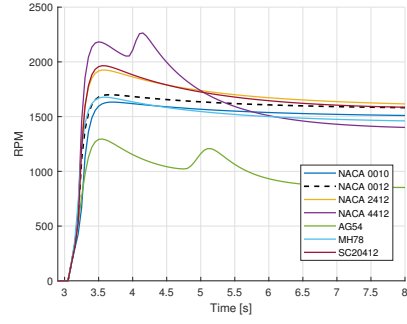
To conclude, the results of the simulations for the linear twist rates from a mathematical model perspective are in accordance with the theory. However, this section opened questions regarding the rotor operation mode and how accurate and what necessary changes should be considered for better modelling and stable flight.

Simulations including several different airfoils were done to understand how the choice of the airfoil affects the rotor performance in autorotation. Cambered airfoils (NACA 2412, 4412) perform better, as they produce more lift at negative angles of attack compared to non-cambered airfoils (NACA 0010, 0012). Descent velocity (Fig. 20(a)) and rotor speed (Fig. 20(b)) confirm these trends. Cambered airfoils reduce the descent rate more than symmetric ones. AG54 also shows good performance operating at lower rotor RPM.

Fig. 21(a) shows cambered airfoils producing higher thrust, which explains improved descent performance. Rotor torque (Fig. 21(b)) confirms that
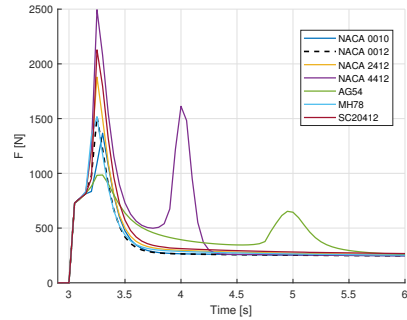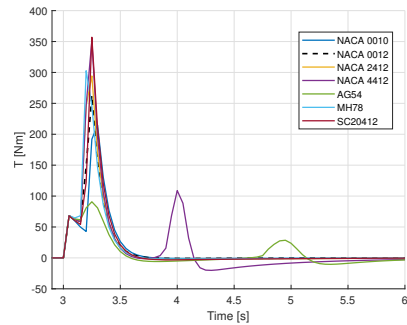
autorotation has reached the VRS.

Figure 21: Rotor's force in N (a); and torque in Nm (b), for different airfoils

In summary, camber improves rotor performance during autorotation. AG54 performs well and may

8

be suitable for recovery systems. Airfoil choice has a clear impact on vehicle descent and rotor dynamics.

9. Autorotation under the influence of wind gust

To study how wind gusts affect the rotor, it is assumed a horizontal wind acting along the x-axis. This wind represents a sudden push forward at constant speed and duration, starting after the rotor fully reaches the autorotation. The gust wind effect is studied for four, combining different wind speeds (V_{wind}) and durations (Δt_{wind}). This simplified model captures key effects without adding complexity.

Without wind, the rotor flies axially with constant forward speed since the aerodynamic load is axisymmetric. However, once the gust starts, the rotor generates starts to be pushed forward. This increases the vehicle's forward speed (Fig. 22).
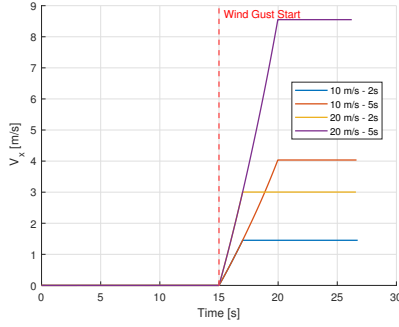

Figure 22: Forward velocity, in m/s, under wind gust

The gust makes the vehicle glide, in other words, moving forward and continues descending. Stronger gusts push harder, increasing the forward velocity. As forward speed increases, the rotor enters a less efficient flow state. This reduces lift. Fig. 23 shows that lift drops more rapidly when the wind is stronger. Consequently, the vehicle descends with a higher velocity (Fig. 25).
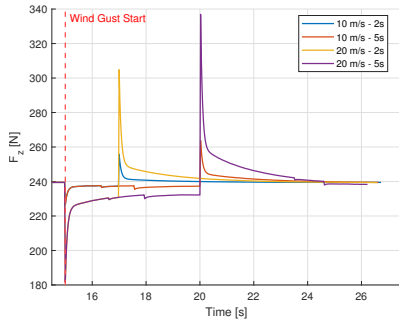

Figure 23: Rotor lift force under wind gust

At the start of the gust, the rotor also loses torque (Fig. 24), causing a short drop in rotor RPM (Fig. 26). This temporarily reduces lift. But as the
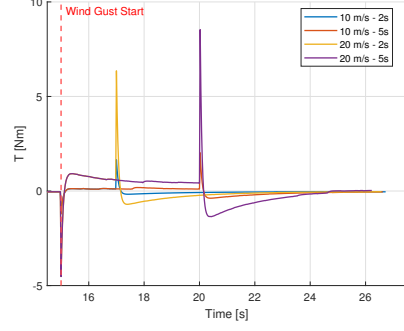

Figure 24: Rotor torque under wind gust

descent speed increases, the rotor speeds up again and recovers torque and lift. At the end of the gust, the rotor doesn't fully counteract gravity but tends toward a new steady state. In all cases, it returns to stable autorotation, even after disturbance.
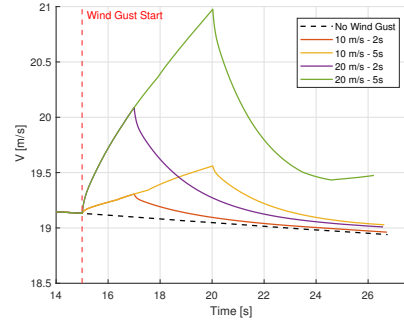

Figure 25: Descent velocity, in m/s, under gust wind

When the gust wind is again turned off, the rotor keeps the forward motion at a constant speed. The rotor is now in a new steady state, a glide flight with a constant descent velocity (Fig. 26).

This proves that autorotation works under glide and enhances its viability for spacecraft recovery.
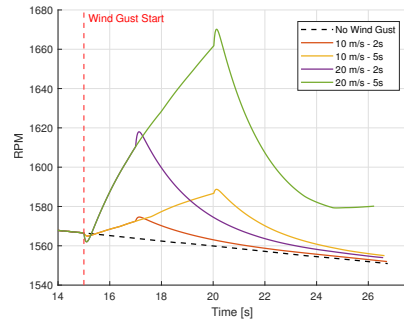

Figure 26: Rotor velocity, in RPM, under gust wind

10. Conclusions

In an effort to enhance the understanding of autorotation and its viability for space missions, this work advanced rotor recovery applied to spacecraft. Although autorotation has historically been employed

in helicopters as an emergency technique, its usage in spacecraft raises new physical issues, particularly concerning the coupled dynamics between the rotor and the vehicle. By applying BET in forward flight, introducing a 6-DOF framework and improving the aerodynamic model, this work enhanced both the vehicle and rotor models, building on the earlier work of Marques [13]. A simulator was created to facilitate further research, and the aerodynamic model was improved using an extrapolation technique and a neural network (NN) to lower computational costs while enhancing accuracy.

To evaluate the effects of taper, blade twist, and root cut-out on rotor performance in autorotation, a parametric research was conducted. According to the results, twist needs to be managed to prevent unstable regimes like the VRS, and lower root cutout and taper constants can help keep the rotor working in slow descent. The choice of airfoil also had an impact on rotor behaviour, underscoring its significance in the initial design phases. The rotor's promise for spacecraft recovery was supported by its ability to re-establish stable autorotation following wind gust disturbances. The project is still in its early stages, and further research is needed to refine the models and enhance validation efforts, even if all suggested objectives are met and the results are encouraging.

References

[1] Joana Ribeiro Gomes, Tessaleno Campos Devezas, Mischel Carmen Belderrain, and Maria Cristina Vilela Salgado. The Road to Privatization of Space Exploration: What is Missing? *64th International Astronautical Congress*, 2013.

[2] Nicola Garzaniti, Zeljko Tekic, Dragan Kukolj, and Alessandro Golkar. Review of technology trends in new space missions using a patent analytics approach. *Progress in Aerospace Sciences*, 125:100727, August 2021.

[3] Mohamed Ragab and F. McNeil Cheatwood. Launch Vehicle Recovery and Reuse. In *AIAA SPACE 2015 Conference and Exposition*, Pasadena, California, August 2015. American Institute of Aeronautics and Astronautics.

[4] Ricardo A. Diaz-Silva, Daniel Arellano, Martinus Sarigulklijn, and Nesrin Sarigul-Klijn. Rotary Decelerators for Spacecraft: Historical Review and Simulation Results. In *AIAA SPACE 2013 Conference and Exposition*, San Diego, CA, September 2013. American Institute of Aeronautics and Astronautics.

[5] R.F Wernicke. Preliminary Tests of Model Spacecraft Rotor Landing System. Technical report, Bell Helicopter Corporation, 1959.

[6] Justin Barzda. Rotors for Recovery. In *Entry Technology Conference*, Williamsburg and Hampton,VA,U.S.A., October 1964. American Institute of Aeronautics and Astronautics.

[7] Dario Modenini. ARMADA: Autorotation, Feasible Alternative to Traditional Martian Entry, Descent and Landing. January 2009.

[8] Clemens Riegler, Ivaylo Angelov, Florian Kohmann, Tobias Neumann, Abdurrahman Bilican, Jessica Gutierrez Pielucha, Alexander Bohm, Barbara Fischbach, Tim Appelt, Lisa Willand, Oliver Wizemann, Sarah Menninger, Christoph Frohlich, Christian Plausonig, Alexander Hartl, Patrick Kappl, and Reinhard Rath. Project Daedalus, Rotor Controlled Descent And Landing on REXUS23. 2019.

[9] J. Gordon Leishman. *Principles of helicopter aerodynamics*. Number 18 in Cambridge aerospace series. Cambridge University press, Cambridge, 2nd ed edition, 2006.

[10] Peter Sharpe and R John Hansman. NeuralFoil: An Airfoil Aerodynamics Analysis Tool Using Physics-Informed Machine Learning.

[11] David A Spera and Jacobs Technology. Models of Lift and Drag Coefficients of Stalled and Unstalled Airfoils in Wind Turbines and Wind Tunnels. 2008.

[12] Anne Brindejonc, Jayant Sirohi, and Inderjit Chopra. Design and Testing of an Autorotative Payload Delivery System. *Journal of the American Helicopter Society*, 52(4):360, 2007.

[13] João Pedro Caldeira De Sousa Marques, Alain De Souza, and Filipe Szolnoky Cunha. Design of a Helicopter System Recovery for a Sounding Rocket. *International Journal of Aeronautical and Space Sciences*, 25(2):662–675, April 2024.

[14] Dong Han, Vasileios Pastrikakis, and George N. Barakos. Helicopter performance improvement by variable rotor speed and variable blade twist. *Aerospace Science and Technology*, 54:164–173, July 2016.

[15] Dario Modenini, Alessandro Rossetti, and Alessandro Talamelli. Aerodynamic assessment of a rotary entry vehicle for Mars landing: an experimental analysis. *Meccanica*, 54(7):967–984, May 2019.